Numerical Simulation of Lunar Seismic Wave Propagation: Investigation of Subsurface Scattering Properties Near Apollo 12 Landing Site

K. Onodera, T. Kawamura, S. Tanaka, Y. Ishihara, T. Maeda

JGR Planets

RESEARCH ARTICLE
10.1029/2020JE006406

Key Points:

- We simulated impact-induced seismic waves on the Moon considering both scattering effects due to topography and subsurface heterogeneity
- Two different scales of heterogeneity result in better modeling of the scattering structure of the upper lunar crust
- Significant scattering structure is present around the Apollo 12 landing site down to 10-20 km depth

Supporting Information:

- Supporting Information S1

Correspondence to:
K. Onodera,
onodera@ipgp.fr

Citation:
Onodera, K., Kawamura, T., Tanaka, S., Ishihara, Y., & Maeda, T. (2021). Numerical simulation of lunar seismic wave propagation: Investigation of subsurface scattering properties near Apollo 12 landing site. *Journal of Geophysical Research: Planets*, *126*, e2020JE006406. https://doi.org/10.1029/2020JE006406

Received 1 FEB 2020
Accepted 2 FEB 2021

Author Contributions:
Conceptualization: K. Onodera, T. Kawamura, Y. Ishihara
Formal analysis: K. Onodera
Methodology: K. Onodera
Supervision: T. Kawamura, S. Tanaka, Y. Ishihara, T. Maeda
Writing – original draft: K. Onodera
Writing – review & editing: T. Kawamura, S. Tanaka, Y. Ishihara, T. Maeda

Numerical Simulation of Lunar Seismic Wave Propagation: Investigation of Subsurface Scattering Properties Near Apollo 12 Landing Site

K. Onodera[1,2,3], T. Kawamura[1], S. Tanaka[2,3,4], Y. Ishihara[5], and T. Maeda[6]

[1]Institut de Physique du Globe de Paris – Université de Paris, Paris, France, [2]Department of Space and Astronautical Science, School of Physical Sciences, The Graduate University for Advanced Studies, SOKENDAI, Sagamihara, Kanagawa, Japan, [3]Institute of Space and Astronautical Science, Japan Aerospace Exploration Agency, Sagamihara, Kanagawa, Japan, [4]Department of Complexity Science and Engineering, University of Tokyo, Kashiwa, Chiba, Japan, [5]JAXA Space Exploration Center (JSEC), Japan Aerospace Exploration Agency, Sagamihara, Kanagawa, Japan, [6]Graduate School of Science and Technology, Hirosaki University, Hirosaki, Aomori, Japan

Abstract One of the most critical issues associated with the analysis of lunar seismic data is the intense scattering, which prevents precise seismic phase identifications, thereby resulting in poor constraints on the internal structure of the Moon. Although some studies estimated subsurface scattering properties from analyses of the Apollo seismic data, the properties have large uncertainties and are still open issues to be resolved to improve the inner structure model of the Moon. While the previous studies tried to constrain the scattering features within the lunar crust mainly from data analysis, this study estimated them from a numerical approach. We constrained the scattering properties near Apollo 12 landing site by conducting seismic wave propagation simulations under various parameter settings and comparing the synthetics with the data. As a result, we succeeded in reproducing seismic signals excited by the Apollo artificial impacts. This led to a constraint on the scattering properties, such as typical scale and thickness of heterogeneity, around the Apollo 12 landing site. The derived structure suggests that the intense scattering structure exists down to 20 km at the northern portion of the region of the Apollo 12 landing site, and to 10 km at the southern region from the landing site. In addition, our model requires a smaller P- and S-wave velocity ratio (1.2–1.4) compared with those conventionally considered (>1.73). This implies a dry and porous environment consistent with laboratory measurements of terrestrial samples and reasonable with the generalized lunar environment.

Plain Language Summary A long-duration and spindle shape characterizes the lunar seismic signals observed by the Apollo seismometers. The moonquakes typically last for 1 or 2 h, and the shape of the seismic wave reflects the internal environment of the Moon. From previous studies, these characteristics are estimated to be due to the subsurface fractured structure resultant from the continuous meteoroid impacts over a long period. Generally, it is required to precisely read seismic phases, like P or S, to determine a planetary inner structure. However, for the lunar case, it becomes more difficult to pick up the precise information because almost all phases are covered with intense seismic scattering, resulting in large uncertainties in the lunar internal structure. Therefore, it is paramount to reveal the scattering structure for a better understanding of the lunar seismic features and the inner structure. This study constrains the subsurface scattering structure around Apollo 12 landing site by modeling the Apollo seismic waves using numerical simulation of seismic wave propagation. Our simulations for various inner structure settings resulted in reproducing the Apollo seismic records very well, leading to constraining the scattering structure around the Apollo 12 landing site.

1. Introduction

In the Apollo 11, 12, 14, 15, and 16 missions, seismometers were deployed on the near side of the Moon with the goal to investigate the internal structure. So far, several one-dimensional internal structure models have been proposed using relatively high S/N seismic data of moonquakes and both natural and artificial impacts (e.g., Gagnepain-Beyneix et al., 2006; Garcia et al., 2011; Khan et al., 2000; Lognonné et al., 2003; Nakamura et al., 1983; Weber et al., 2011). However, these models show some discrepancies, and sometimes

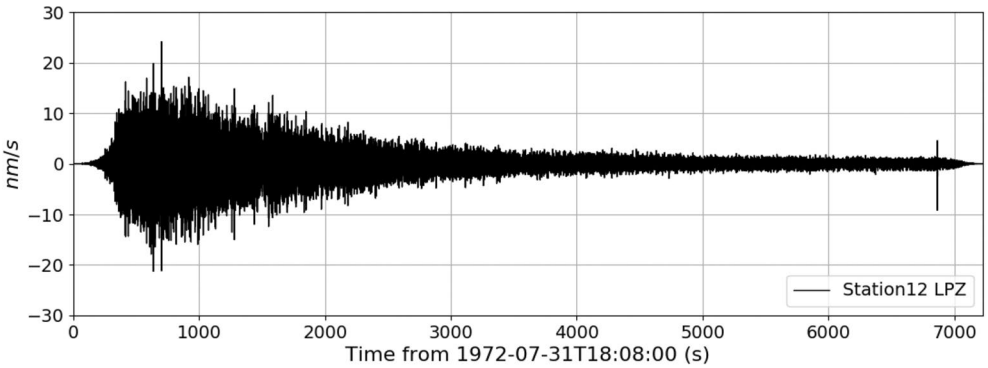

Figure 1. An example of the lunar seismic waveform induced by a meteoroid impact which occurred on July 31, 1972.

the differences exceed their error bars, implying that a similar data set may have different interpretations. In other words, it is considered that the Apollo lunar seismic data do not have good quality enough to constrain the internal structure precisely.

Generally, a lunar seismic waveform has an ambient arrival and builds up gradually to the peak, then experiences a long decay (typically a few hours; Figure 1; e.g., Latham et al., 1970; Toksöz et al., 1974). This characteristic trend is considered to be attributed to the intense scattering at subsurface fractured layers, called the regolith and megaregolith (e.g., Blanchette-Guertin et al., 2012). Owing to this intense scattering, it becomes difficult to precisely read arrival times of seismic phases, thereby resulting in poorly constrained models of the inner structure. While arrival times can be read with a precision of about 0.1 s for the Earth seismic records, the reading error becomes 10–100 times worse than those of the Earth for the lunar case (e.g., Lognonné et al., 2003). Thus, the intense seismic scattering is clearly one of the most critical issues needed to be overcome to construct more reliable models of the lunar internal structure.

For the scattering of the regolith, several studies have been conducted with different approaches (laboratory experiments [e.g., Dainty et al., 1974], data analysis of the Apollo seismic signals [e.g., Blanchette-Guertin et al., 2012; Cooper et al., 1974; Dainty et al., 1974; Gillet et al., 2017], and numerical simulation [e.g., Blanchette-Guertin et al., 2015]). For example, Cooper et al. (1974) estimated the velocity structure up to about 2.0 km depth using seismic signals generated by explosions in the Apollo 17 lunar seismic profiling experiment (LSPE). Heffels et al. (2017) re-analyzed the LSPE data combined with the refined coordinates by Hasse et al. (2013). They concluded that the uppermost layers, called the regolith layers, consist of fine grains and fractured rocks with low elastic velocity (200 m/s–2.8 km/s) down to at least 2.0 km depth.

In terms of the deeper scattering structure, Dainty et al. (1974) introduced diffusion theory and attempted to fit the shape of the scattering coda for the Apollo artificial impacts and deep moonquakes, thus resulting in the constraint on the diffusivity of seismic energy within the crust. Based on their analyses, the scattering layer with several km-scale scattering media—the so-called megaregolith—appears to exist up to 10–25 km depth. However, the diffusion equation they introduced is not good enough to fit the energy growth trend of the lunar seismic waves, especially at the rise-coda part—the build-up part of energy from the first arrival to its maximum energy arrival. As the scattering features are more dominantly reflected in rise-coda than in decay-coda (Gillet et al., 2017), diffusion theory does not seem to work in constraining scattering properties such as heterogeneity size and density fluctuation.

Concerning the megaregolith, the recent studies suggested its importance on the lunar seismic scattering. Blanchette-Guertin et al. (2012) evaluated the quality factor Q systematically by analyzing four different types of events—artificial impacts, natural impacts, shallow moonquakes, and deep moonquakes—for different frequency bands. Their results indicate that the scattering media with heterogeneities of 30–200 m scale exists up to several km depth, and imply that this kind of heterogeneities has dominant effects on the propagation of seismic waves observable with the Apollo long period (LP: ~0.15 s sampling) and short period (SP: ~0.02 s sampling) seismometers. Moreover, more recently, Gillet et al. (2017) obtained a much thicker megaregolith. They investigated the rise-time—the time from the first arrival to the maximum energy arrival—and the decay-time—the time for energy decay from the maximum energy arrival to noise floor—

of lunar seismograms to quantify the scattering and the intrinsic Q as well as the diffusivity. Interestingly, their results suggest that a 100 km thick megaregolith is necessary to explain the lunar seismic coda despite 20–25 km depth was proposed as an upper limit in the previous studies (e.g., Han et al., 2014; Jaumann et al., 2012). Although some studies estimated the scattering properties of the megaregolith, its characteristics are still open issues (Jaumann et al., 2012). The scattering features of the megaregolith are paramount to understand not only the lunar internal structure but also the formation process of heterogeneity within the crust, which is useful to discuss the evolution of the lunar and other planetary surface environments (e.g., Blanchette-Guertin et al., 2012). Thus, constraining the scattering properties of the megaregolith will contribute to the development of seismology as well as planetary science.

Besides the low-velocity and scattering layer, the local structure, for example, surface and/or Moho topographies, could also contribute to the development of seismic scattering (e.g., Blanchette-Guertin et al., 2012; Onodera et al., 2018). For the Earth seismology, the effect of local topographies on the seismic scattering is paramount (e.g., Kumagai et al., 2011; Sato et al., 2012; Takemura et al., 2015). Since the dynamic range of topographies on extraterrestrial planetary bodies, for example, Moon and Mars, is larger than that of the Earth, topographical effects can be a key factor in interpreting seismic scattering in the field of planetary seismology. However, this point has not been considered extensively so far. In this study, both scattering media and topographies are included in the simulations, hence allowing us to consider both scattering effects.

While the previous studies focused on constraining the scattering properties from a data analysis, we estimate them from a numerical approach. Although some studies conducted numerical simulations (e.g., Blanchette-Guertin et al., 2015), none of them compared the synthetics with the Apollo data in a direct approach. Contrariwise, our simulation succeeded in producing theoretical waveforms identical to the Apollo ones, thereby enabling us to compare the synthetics and the data more directly (e.g., envelope, energy growth trend, and rise-time). In the following section, we introduce a seismological simulation code, then discuss the simulation results, focusing on signal rise-time and seismic energy. Finally, we summarize the model best-fitting the data and discuss its difference from the previously proposed ones.

2. Methodology

2.1. Simulation Code

We used an open-source seismic wave propagation code (OpenSWPC) version 4.3.3 to simulate the impact-induced seismic waves on the Moon. This code was originally developed by Maeda et al. (2017) in order to simulate seismic wave propagation within viscoelastic media. Since this code performs simulations in a Cartesian coordinate system, it cannot perform global-scale simulation for a spherical body. However, in determining the crustal structure, the scale of several hundred km is enough to evaluate its characteristics. In this study, the simulated events' epicentral distance ranges from 150 to 200 km (5.0°–6.6°) and the deepest path of the seismic ray passes about 30 km depth. Therefore, we consider that the OpenSWPC meets our requirements.

Notably, the OpenSWPC's parameters are originally set for the Earth. To apply this code to the Moon, we changed the radius and inverse ellipticity value to the lunar case (radius: 1,737.4 km and inverse ellipticity: 10^{15}) when projecting the lunar coordinates onto the Cartesian coordinates using Gauss-Krüger transform (Kawase, 2011). Concerning the inverse ellipticity, we adopted a large enough value to make it closer to a true sphere (10^{15}).

We performed simulations in a two-dimensional P-SV system, that is, within the vertical plain along each path between a seismic station and an impact point. We located a seismic station at the origin and set the X-axis (horizontal) in the direction of the azimuth from the origin to a seismic source. We set the positive direction of the Z-axis (vertical) downward. For the calculation, we set the grid size to 20 m for both X and Z directions and set the time step to about 0.15 s (6.6 Hz), which corresponds to the sampling rate of the Apollo long period seismometer.

In general, two-dimensional wave-simulation does not correct the difference in geometrical attenuation with the distance between two-dimensional and three-dimensional (Table S1). In the case of body waves, since the relative waveform becomes similar to one another, we consider that the two-dimensional

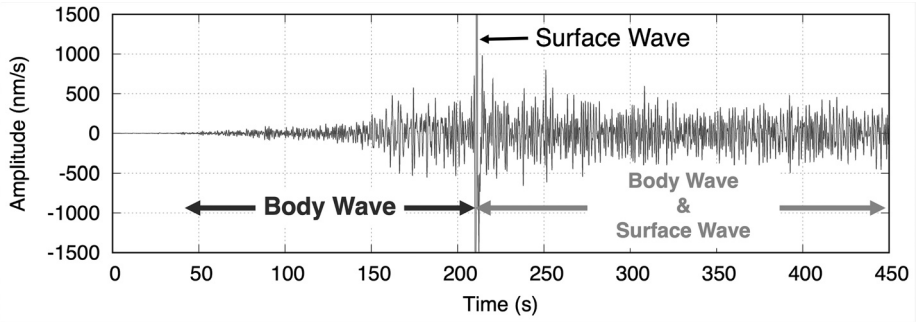

Figure 2. An example of a waveform of an impact-induced seismic wave calculated with two-dimensional simulation is shown. Sharp peak around 210 s corresponds to the onset of the surface wave (Rayleigh wave).

simulation results will not affect our interpretation. However, surface waves simulated in two-dimensional are not attenuated with distance, hence resulting in a strong artificial peak, as seen in Figure 2. Since the energy peak of the lunar seismic waves are due to body waves rather than surface waves at the epicentral distance more than ~100 km (Latham et al., 1971), we focused only on the body waves observed prior to the surface wave arrivals. As the rise-coda strongly reflects the scattering properties of subsurface compared to the decay-coda (e.g., Gillet et al., 2017), the synthetic waves prior to the surface wave arrivals are expected to be enough to assess the scattering properties of the lunar subsurface. To avoid the artificial peak by a surface wave, the wave data from the first arrival to 12 s prior to the artificial peak were used in the following analyses. Besides, since it is not simple to correct the difference in attenuation rates between two-dimensional and three-dimensional for complex structures, for example, multilayer, random media, and topographies, we exclude the discussion on the intensity from this study, that is, we normalized all seismic signals with the maximum amplitude within the target data segment.

2.2. Apollo Artificial Impacts Selected for Simulation

We used the Apollo artificial impacts as references because their impact locations, origin times, and impact parameters are well constrained (Toksöz et al., 1974; Wagner et al., 2017), which is helpful to give the initial source conditions for a simulation. There are two different types of artificial impact. One is the ascent stage of Lunar Module (LM) impact, which was deliberately hit on the lunar surface after the Apollo astronauts left the Moon, and the other is the Saturn IV rocket booster (S-IVB) impact, which was guided to the Moon after its separation from the module section of the Saturn V rocket (Latham et al., 1970; Nakamura et al., 1983). We excluded the LM impacts from this study because their impact angles are so small—less than 10° from the horizon—that is, it is difficult to treat these data with those of the S-IVB impacts in the same way, especially when assuming seismic source conditions. In addition, owing to some constraints from the simulation code and potential problems in the Apollo seismic observation, we ended up selecting two events in Table 1. As for the selection criteria, see the details in Texts S1 and S2. Notably, since the simulation covers the frequency range up to 3.0 Hz, we solely focused on the LP data (peak sensitivity is ~0.4 Hz) instead of those observed with the SP sensor (peak is around 7.0 Hz; Figure S1). We downloaded all the Apollo seismic data used in this study from Data Archives and Transmission System website (https://darts.isas.jaxa.jp/planet/seismology/apollo/index.html).

Table 1
List of Events Used in This Study

Impactor	Receiver	Acronym in this paper	Epicentral distance (km)
Apollo16 S-IVB	Station12 LPZ	A16S12	153.7
Apollo14 S-IVB	Station12 LPZ	A14S12	175.3

2.3. Input Parameters for Simulation

2.3.1. Velocity Structure and Intrinsic Q

We constructed three different velocity models consisting of four layers (the regolith, megaregolith, crust, and mantle). Notably, the discrimination of the regolith and megaregolith is still debated and may differ depending on the parameters we focus on. In this study, we distinguish the regolith from the megaregolith depending on heterogeneity size.

Table 2
Reference Velocity Structures and Intrinsic Q. V_p and V_s Represents Average P-Wave and S-wave Velocity for Each Layer, Respectively. See 2.3.1 for Details

Layer	Density (g/cm^3)	Model 0		Model 1		Model 2		Intrinsic Q	
		V_p (km/s)	V_s (km/s)	V_p (km/s)	V_s (km/s)	V_p (km/s)	V_s (km/s)	Q_p	Q_s
Regolith	2.600*	1.38*	0.80*	1.38*	0.87*	1.38*	1.10*	6,750	6,750
Megaregolith	2.762*	3.20*	1.85*	3.20*	1.76*	3.20*	2.30*	5,000	5,000
Crust	2.762	5.50	3.18	5.50	3.18	5.50	3.18	4,000	4,000
Mantle	3.360	7.55	4.36	7.55	4.36	7.55	4.36	3,750	1,500

V_p and V_s represents average P-wave and S-wave velocity for each layer, respectively. See Section 2.3.1 for details. *Since random media is inserted into the regolith and megaregolith layers, the P-wave velocity and S-wave velocities fluctuate up to 28.0% for the regolith and 14.0% for the megaregolith, respectively, which correspond to 22.4% and 11.2% density fluctuation, respectively.

While the typical scale of scatterers in the regolith has 200 m, 600 m scale heterogeneity was given for the megaregolith.

In each model in Table 2, we used common parameters referred from Garcia et al. (2011) for (1) density and V_p (P-wave velocity) in all layers; (2) V_s (S-wave velocity) in the crust and mantle. Besides, concerning intrinsic Q, we gave the same values to all layers by combining the results of Blanchette-Guertin et al. (2012), Garcia et al., (2011), and Nakamura and Koyama (1982). The main difference among these models is the V_p/V_s ratio in the regolith and megaregolith layers. For Model 0, we assumed a Poisson body ($V_p/V_s = \sqrt{3}$), while the ratio of Model 1 is based on the laboratory measurements of the Apollo 12 returned samples by Kanamori et al. (1971) (1.59 and 1.82 for the regolith and megaregolith). Concerning Model 2, the smaller wave velocity ratio was provided for the regolith (1.25) and the megaregolith (1.39), which we determined based on trials and errors.

For scattering media, we introduced two different scales of heterogeneity to simulate the scattering in the regolith and megaregolith layers. These random media were characterized by exponential power spectral density function (Sato et al., 2012). For the regolith layer, we set the typical scale of random media to 200 m and considered a 28% velocity fluctuation based on the results of Blanchette-Guertin et al. (2012) and Weber et al. (2015). Concerning the megaregolith layer, since there are few established structures, we provided a priori assumptions. Since it is considered that the S-wave scattering is more dominant in the dry and porous environment, we adopted the scale compatible with an S-wave wavelength of 600 m. For velocity fluctuation, we considered a smaller value (14%) than that of the regolith, because the structure becomes less fractured as it tends downward due to confining pressure.

2.3.2. Crustal Structure Settings

We utilized one of the lunar crustal structure models based on the observation by Gravity Recovery and Interior Laboratory (GRAIL) mission (Wieczorek et al., 2013). Out of the proposed models by Wieczorek et al. (2013), we selected Model 2, which was constructed with the spherical harmonic expansions up to 310° with an anchoring condition of the crustal thickness estimated by Lognonné et al. (2003), so that our density model is consistent with that of their model. This model produces an average crustal thickness of about 35 km. We downloaded the original data from the GRAIL Crustal Thickness Archive (https://zenodo.figshare.com/articles/GRAIL_Crustal_Thickness_Archive/6915155/1). Figures 3a and b show the surface and the Moho topography models used in the simulations, respectively.

As mentioned by Jaumann et al. (2012), the structure of the fractured layers is still uncertain. While estimates from seismological studies suggest relatively thick scattering layer in the order of 20–30 km (e.g., Latham et al., 1970; Toksöz et al., 1974) or even 100 km (Gillet et al., 2017), geological observations and theoretical modeling have suggested a much thinner layer (a few hundred meters – 10 km; e.g., Hartmann, 1973; Heiken et al., 1991; McGetchin et al., 1973). This study started with a relatively thin layer of 5 and 10 km for

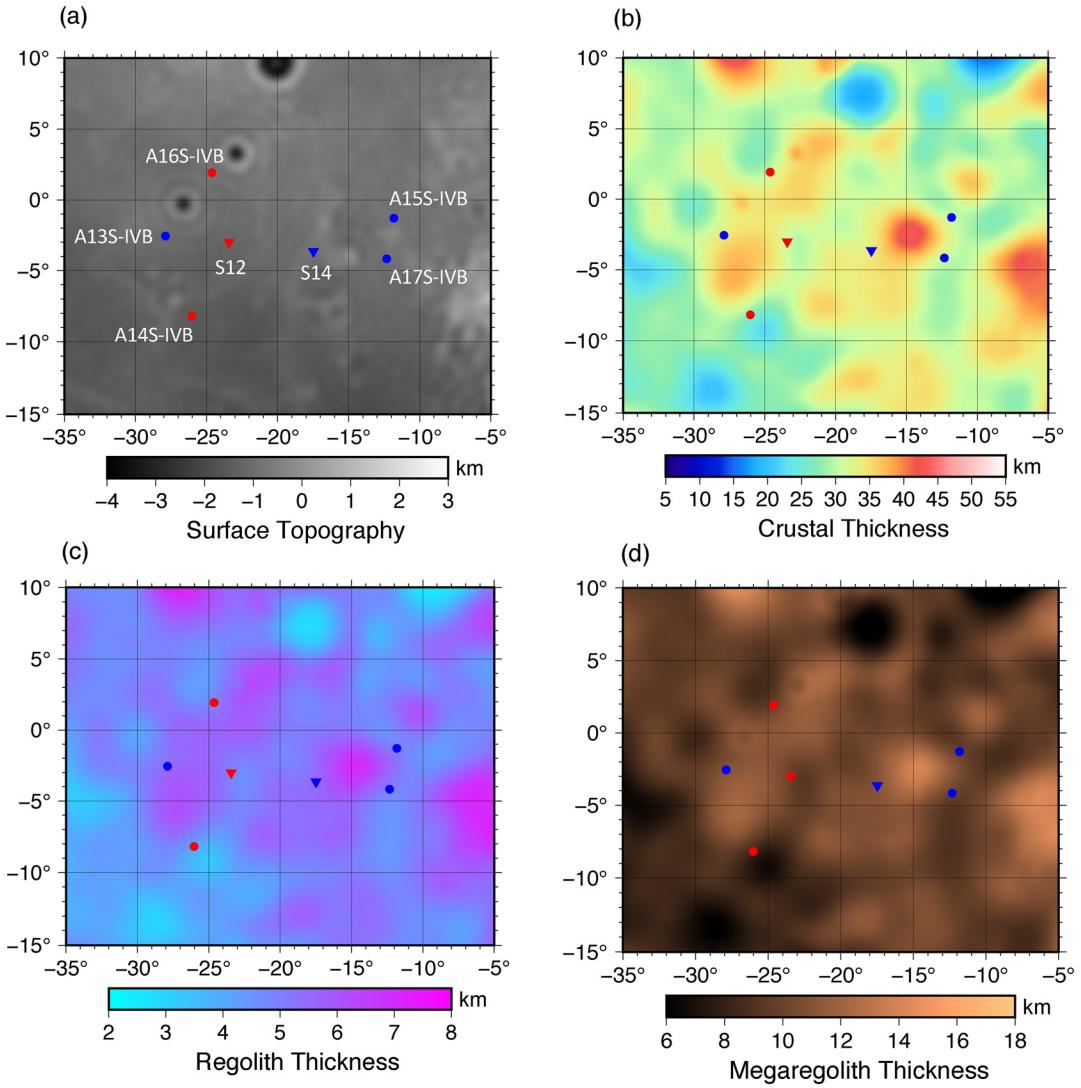

Figure 3. (a) Surface topography model. The inverted triangles show the location of Apollo passive seismic experiment (PSE) and the circles represent the positions of Apollo S-IVB impacts. Those used in this study are colored in red while those unused are in blue. (b) Distribution of crustal thickness. The color scale represents the thickness of crust deduced from GRAIL data by Wieczorek et al. (2013). (c) Distribution of regolith thickness. The color scale shows the layer thickness of regolith in km. (d) Distribution of megaregolith thickness. The color scale shows the layer thickness of megaregolith in km. For (a) and (b), we downloaded the original data from the GRAIL Crustal Thickness Archive (https://zenodo.figshare.com/articles/GRAIL_Crustal_Thickness_Archive/6915155/1). GRAIL, Gravity Recovery and Interior Laboratory; S-IVB, Saturn IV rocket booster.

the regolith and megaregolith, respectively (Heiken et al., 1991). In the latter section, we extend the scattering layer to 20 km depth to observe the influence on the resulting waveforms.

We modeled the regolith and megaregolith structures as follows:

$$D_{\mathrm{reg}}\left(x,y\right) = D_{\mathrm{surf}}\left(x,y\right) + \frac{\left(D_{\mathrm{crust}}\left(x,y\right) - D_{\mathrm{surf}}\left(x,y\right)\right)}{C_1} \tag{1}$$

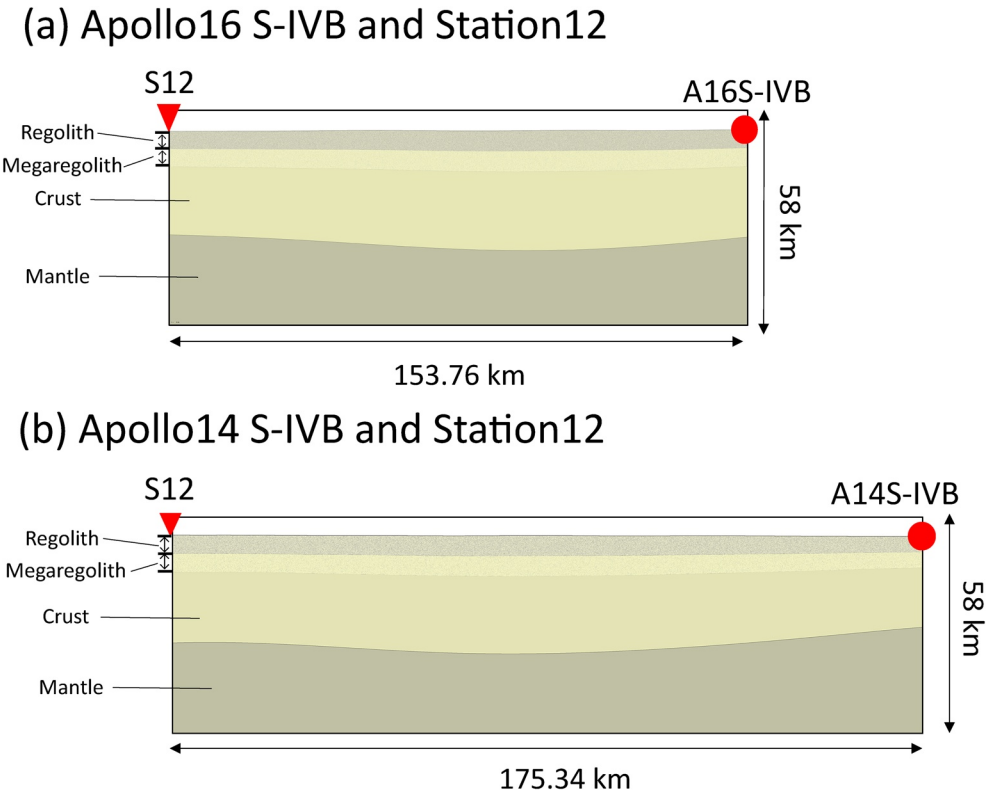

Figure 4. Vertical plain between impact point and the Apollo station (a) Apollo16 S-IVB impact and Station12; (b) Apollo14 S-IVB impact and Station12. S represents Station while AXS-IV represents Apollo X S-IVB impact, respectively. S-IVB, Saturn IV rocket booster.

$$D_{\mathrm{Mreg}}\left(x,y\right)=D_{\mathrm{surf}}\left(x,y\right)+\frac{\left(D_{\mathrm{crust}}\left(x,y\right)-D_{\mathrm{surf}}\left(x,y\right)\right)}{C_2} \tag{2}$$

where x and y represents longitude and latitude ($-40° < x < 0°$, $-20° < y < 20°$), and D_{surf}, D_{crust}, D_{reg}, and D_{Mreg} correspond to the depth of each boundary from the lunar mean radius to the surface boundary, surface-Moho boundary, regolith-megaregolith boundary, megaregolith-crust boundary, respectively. C_1 and C_2 are constants that make the average thickness of the regolith and megaregolith to be 5 and 10 km, respectively, near the Apollo 12 and 14 landing sites ($C_1 = 5.84$, $C_2 = 2.92$), resulting in the distribution shown in Figures 3c and d. Figure 4 illustrates the vertical plain along each event listed in Table 1. For the Apollo16 S-IVB and Station12 case (subsequently referred to as A16S12), the crustal thickness beneath both station and impact point is identical, and Moho undulation is about 5 km. For Apollo14 S-IVB and Station12 case (A14S12), while the Moho undulation is compatible with that of A16S12 case, it has relatively thinner crust at the impact point (~25 km).

2.3.3. Seismic Source Assumption for Impact

As discussed by the previous studies (e.g., Melosh, 1989; Teanby & Wookey, 2011), impacts are considered as an analog of explosions. Following the assumptions made by some numerical studies on impact-induced seismic wave (Blanchette-Guertin et al., 2015; I. Daubar et al., 2018; I. J. Daubar et al., 2020), the seismic source which isotropically radiates P-waves was placed at one grid point below the surface. This means that all components of the moment tensor are equal to 0 except the diagonal components. Since the intensity is normalized, $M_{ii} = 1/\sqrt{3}\left(i = 1,2,3\right)$. We assumed a source time function (STF) proposed by Gudkova et al. (2011) and (2015) who estimated the STF of the Apollo S-IVB impacts from spectral analysis of Apollo

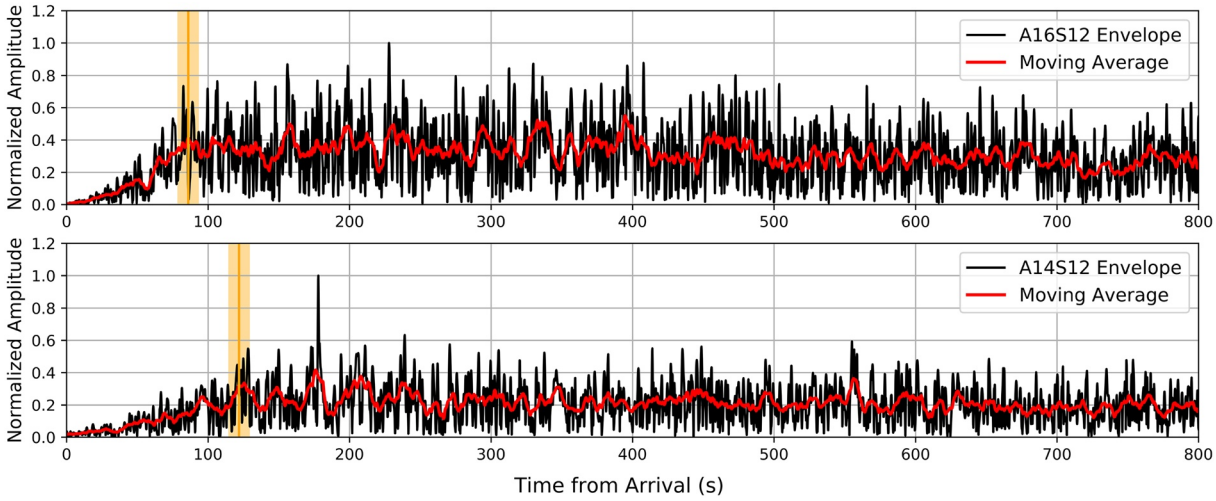

Figure 5. Smoothed envelopes of the two Apollo artificial impacts data considered in this study. Horizontal axis shows time from first arrival. The arrival times of Apollo artificial impacts were referred from Lognonné et al. (2003). Each signal is normalized with the maximum amplitude of each filtered Apollo envelope shown in black. The red lines show the smoothed envelopes with time windows of 7.5 s (50 samples). The vertical yellow lines represent the rise-time for each event with error bars of 7.5 s.

seismic data. This STF has a characteristic time scale of 0.65 s, resulting in the dominant frequency around 1.5 Hz (Figure S3).

2.4. Energy Peak Arrival

In the analysis, the Apollo seismic data were converted from digital unit to velocity using ObsPy (Beyreuther et al., 2010). We calculated the poles and zeroes based on the information by Horvath (1979) and Yamamoto et al. (2019). After that, we filtered the velocity signals using the fourth order of Butterworth filter with the frequency range between 0.2 and 1.5 Hz at which the sensitivity of LP peaked mode attains its maximum. We also applied the same bandpass filter to the velocity signals of synthetic waves, allowing us to compare with the data in the same physical unit and frequency range.

To read the rise-time, we smoothed the seismic signals with a 7.5 s time window. This study used a relatively smaller time window compared to previous studies (e.g., 20 s; Gillet et al., 2017) to look into smaller signal variation of the rise-coda. The rise-times were read by searching the point that the amplitude reaches around the maximum and stabilizes. Figure 5 illustrates the estimated rise-times for the Apollo data.

3. Results

First, we compare the simulation results with the Apollo data in terms of rise-time arrival and see which model is preferable to explain the data. Second, we show the results for additional simulations in which several patterns of scattering layers' thickness were varied to observe whether rise-time can be better matched from the first proposed models. Finally, we determine the best velocity model for each event case from the comparison of trend of coda energy with time.

3.1. Rise-Time Arrival

Figure 6 compares the rise-time arrivals of simulations for Models 0–2 with that of the Apollo data. While the Apollo data of A16S12 and S14S12 show the rise-time of ~85 s and ~120 s, respectively, those for simulations are delayed by about 30–40 s from the data. From the comparison among velocity structure models, it seems that Models 1 and 2 show smaller discrepancies with the data compared with Model 0. Considering that Models 1 and 2 have larger V_s than Model 0 (i.e., smaller V_p/V_s ratio), the S-wave component plays a paramount role in determining the rise-time. As suggested by Lee (2003) and Sato et al. (2012), the V_p/V_s ratio becomes smaller under the dry and porous environment. Basically, this trend is also consistent with

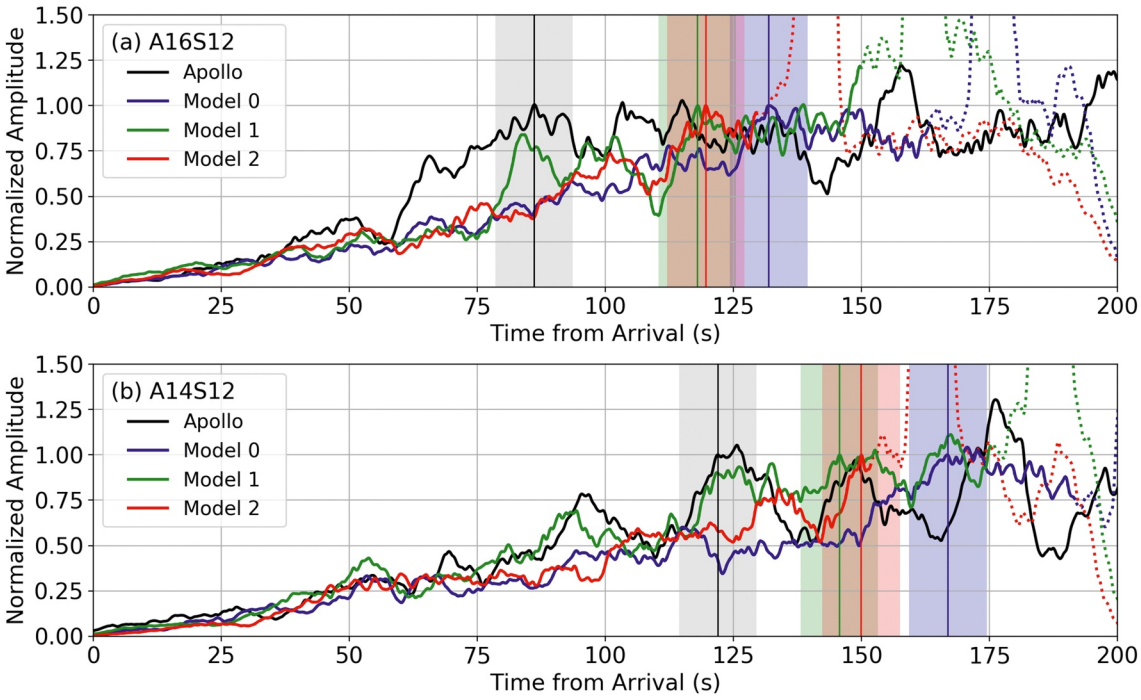

Figure 6. Rise time readings of (a) A16S12 and (b) A14S12 cases. We scaled each envelope is scaled with the amplitude at each rise time. The black, blue, green, and red envelopes are smoothed envelopes of the Apollo, Model 0, Model 1, and Model 2, respectively. Note that the envelopes beyond the analysis window are shown in the dotted line. The colored vertical lines with shade show the rise-time with a 7.5 s error.

some measurements of the Apollo samples (e.g., Kanamori et al., 1970, 1971). Our results that the smaller elastic velocity ratios can better explain the lunar seismic data are more consistent with our understanding that the Moon is drier than the Earth.

Next, in order to fit the rise-time better, we conducted additional simulations under different layer-thickness of the regolith and megaregolith, especially for Models 1 and 2. Here, we changed only the thickness of the scattering layers (Table 3). We set the average boundary depth from the surface to 2.5, 5.0, and 7.5 km for the regolith and to 10 and 20 km for the megaregolith. Notably, that the other parameters besides the thickness of the scattering layers (e.g., P-wave, S-wave, and intrinsic Q) are the same as those listed in Table 2.

Figure 7 shows the results of the rise-time readings for the additional simulations. In both cases (A16S12 and A14S12), a thicker scattering layer (~20 km) relatively worked well to reduce the discrepancy of rise-times between the simulations and data (i.e., the rise-time matches the data within the error bar). In addition, the Model 2 cases appear to better fit the rise-time than the Model 1 cases. As an example of A16S12, taking the average difference of the rise-time between the data and simulation, Model 1 has a time-offset of 40.1 s while Model 2 has 23.6 s. The same trend is seen for A14S12 case. Since the Model 2 has larger S-wave velocity and its P-wave velocity is fixed, the smaller elastic velocity ratio seems preferable for explaining the Apollo data. By focusing on reconciling the rise-time, Model 2 fits the data better, and a thicker layer of 20 km is required. To quantitatively evaluate which model is the best, we compare the synthetics and the data in terms of energy in the next section.

Table 3
Structure Settings for Additional Simulations

Model (X = 1, 2)	Regolith boundary depth (km)	Megaregolith boundary depth (km)
Model X-1	2.5	10
Model X-2	5.0	10
Model X-3	7.5	10
Model X-4	2.5	20
Model X-5	5.0	20
Model X-6	7.5	20

3.2. Comparison of Energy Growth Trend

In addition to the rise-time, we investigated the seismic energy as it is an important criterion to assess if the synthetics are identical to the data. Since the seismic energy is proportional to the squared amplitude, we calculated the equivalent seismic energy for the models consistent with the rise-time of the Apollo within the error bars. Notably, since the rise-times

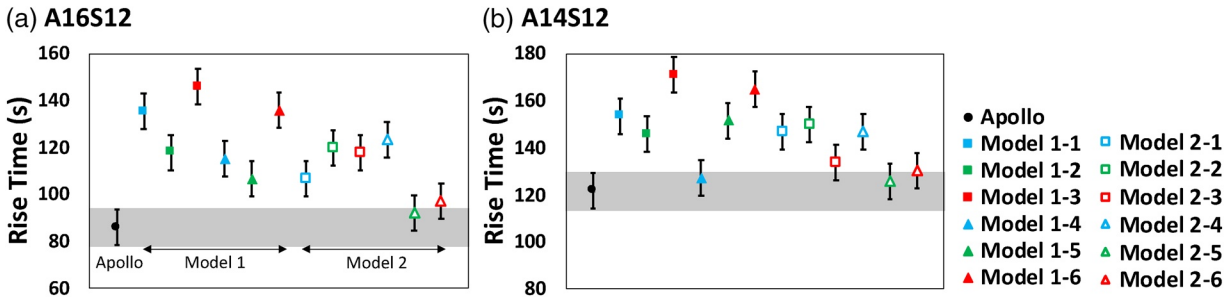

Figure 7. Plots of the rise-time for the simulations and the Apollo for each event case (a) A16S12, (b) A14S12. The colored filled symbols are for Model 1 velocity model cases and the open ones for Model 2 cases. Regarding the symbol color, black corresponds to the Apollo data, blue to 2.5 km regolith case, green to 5.0 km regolith case, and red to 7.5 km case. For symbol shape, the point plots correspond to the Apollo, squared plots to the models of 10 km megaregolith-boundary depth, and triangles to 20 km cases. We determined error bars from the time window for the moving average of envelopes (7.5 s). Gray shade represents the error range of the Apollo rise-time. Table S2 summarizes the values for the figure.

slightly differ among the results, we used the equivalent energy density (EED) in time domain, which is expressed as follows:

$$EED = \sum_{t=0}^{T_{\mathrm{rise}}} A_{\mathrm{env}}(t)^2 \,/\, T_{\mathrm{rise}} \tag{3}$$

where A_{env} represents the amplitude of smoothed envelope, t is time, and T_{rise} corresponds to rise-time. In addition, we also calculated the EED every 10% of T_{rise} for each model in order to observe the time variation of energy fitting.

As a quantitative criterion for the determination of the best model, we calculate the average of absolute value of error (AAE), which is given by:

$$AAE = \sum_{\tau=0.1}^{1.0} \left| 1 - \frac{EED_{\mathrm{sim}}(\tau)}{EED_{\mathrm{Apo}}(\tau)} \right| / N \quad \left(\tau = t \,/\, T_{\mathrm{rise}}\right) \tag{4}$$

where EED_{sim} and EED_{Apo} are the equivalent energy densities for the simulations and the Apollo, respectively, and N is the sample number. As the AAE is calculated every 10% of T_{rise}, $N = 10$ for this study. In this study, we selected the model that has the smallest AAE as the best structure among the models fitting the Apollo rise-time.

The left column of Figure 8 shows the time variation of EEDs scaled with the Apollo ones, and the right column displays the envelopes of the Apollo and the best simulation model for each event case (Models 2–6 for A16S12, Models 2–3 for A14S12). For A16S12 (Figure 8a), while Models 2–5 takes 70%–80% energy ratio in average, Models 2–6 is more consistent with the Apollo data (90%–105%) when $\tau > 0.3$, indicating Models 2–6 is more preferable to explain the Apollo envelope. In the case of A14S12, it seems both Models 1–4 and 2–6 are lack of energy until they reach the rise-times. On the other hand, Models 2–3 and 2–5 have larger EEDs especially over $\tau = 0.4$. While Models 2–5's EED remains excess over that of Apollo till it reaches the rise-time, Models 2–3 shows good agreement with the Apollo between $\tau = 0.8 \sim 1.0$, resulting in the smaller AAE by the half of the other models. In summary, Models 2–6 is preferable for A16S12 case and Models 2–3 better for the case of A14S12.

4. Scattering Structure Around Apollo 12 Landing Site

From the best-fitting results of our simulations (Models 2–3 and 2–6 for A14S12 and A16S12 cases, respectively), we propose the scattering structure in the vicinity of the Apollo 12 landing site. Considering that A14S12 path runs from the southern portion of the region from the Apollo 12 landing site, Models 2–3 corresponds to a representative structure of Mare Cognitum (Figure S2). On the contrary, as A16S12 path comes from northern region from the landing site, Models 2–6 might represent the structure for Mare

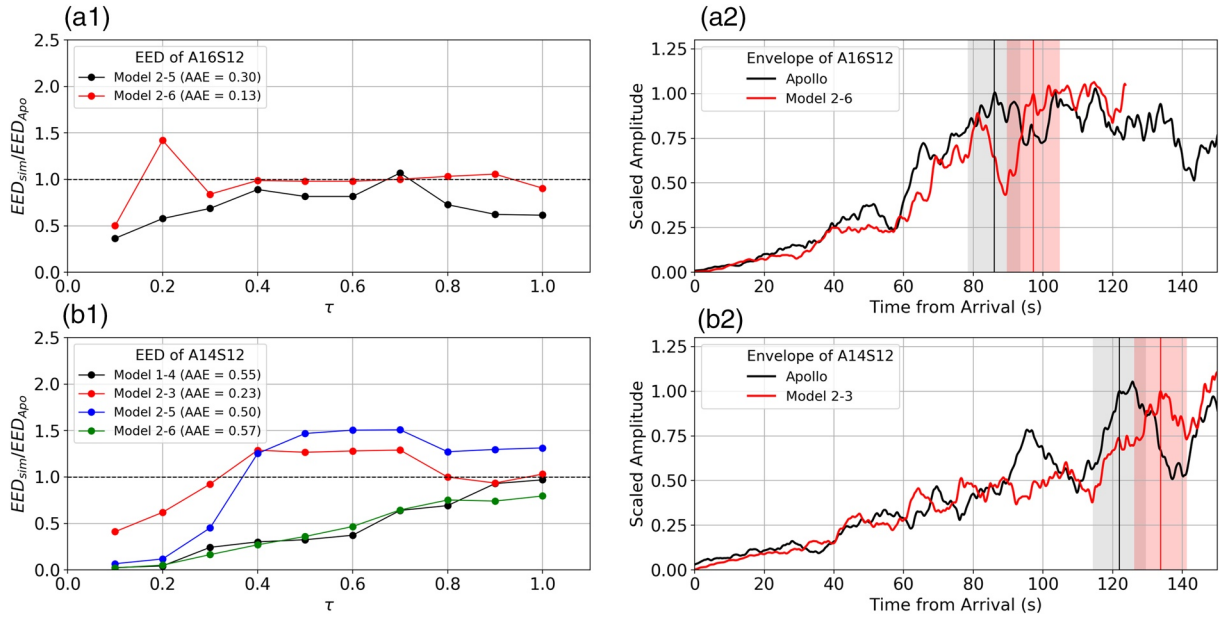

Figure 8. (Left column: a-1 and b-1) Time variation of EED. We calculated EEDs every 10 % of T_{rise} and scaled them with those of Apollo. (Right column: a-2 and b-2) Envelopes for the best cases. Each black envelope corresponds to the Apollo and red to the best cases. We normalized all envelopes with the amplitude at each rise-time. The vertical lines with shade show the rise-times and their errors. EED, equivalent energy density; EEDs, equivalent energy densities.

Insularum (Figure S2). In these regions, the subsurface structure could be modeled with two different scales of scattering media. One is the 200-m-scale scatterers with 28 % velocity fluctuation, and the other underlying layer consists of the 600-m-scale heterogeneity with 14% velocity fluctuation. The first scattering layer (we call it as the regolith) is 7.5 km thick in both regions, whereas the second layer (the megaregolith in this study) continues down to 10 or 20 km depth depending on the path.

In the Oceanus Procellarum including both regions of interest (Mare Cognitum and Mare Insularum), the thin basalt layer (0.4–1.0 km; Gong et al., 2016) covers the ejecta blanket from Mare Imbrium (Figure S2), which is thought to be placed on the underlying anorthosite crust (Swann et al., 1971). Moreover, considering that the crater depth of Copernicus (Figure S2) is about 4 km depth and the different material can be confirmed inside (Swann et al., 1971), the total thickness of the basalt and the underlying ejecta layers seems to be equivalent to the order of the crater depth. Thus, we consider that the first scattering layer mainly shows the mixed scattering properties of the basalt and the ejecta layers, while the second layer exhibits that of the underlying crust. Regarding the second scattering layer, we can observe a difference between the northern and southern path. The results tell us that the northern path requires thicker scattering layer than the southern one. As this trend is consistent with the distribution of the crustal thickness shown in Figure 3b, the difference in the second scattering layer might reflect the lateral variation of the crust.

Figure 9 compares our velocity structure models with those previously proposed. Note that our models (Models 2–3 and 2–6) are representative structures for Mare Cognitum and Mare Insularum, respectively (Figure S2) while other studies show those for the wider range of region (such as near-side of the Moon). Our models have the lower velocity layer up to several km depth compared to other ones, whereas the velocity profile is relatively consistent with each other at the deeper part (>10–20 km). Regarding the V_p/V_s ratio, we find that our results require a smaller ratio (1.25 and 1.39 for the regolith and megaregolith, respectively) than the previous models (>1.7 by Lognonné et al., 2003; Nakamura et al., 1983). As the environment becomes drier and more porous, the V_p/V_s ratio becomes smaller (Lee, 2003; Sato et al., 2012). Therefore, our results seem consistent with the laboratory measurements as well as our understandings on the lunar environment. In general, it is more difficult to read the S-wave arrivals precisely from the Apollo seismic data compared to the P-wave arrivals and usually the uncertainty of the S-phase reading becomes larger (e.g., Ganepain-Beyneix et al., 2006; Lognonné et al., 2003). Since our numerical approach focused on the relation between the elastic velocity ratio and the shape of envelope, it allows us to discuss the S-wave

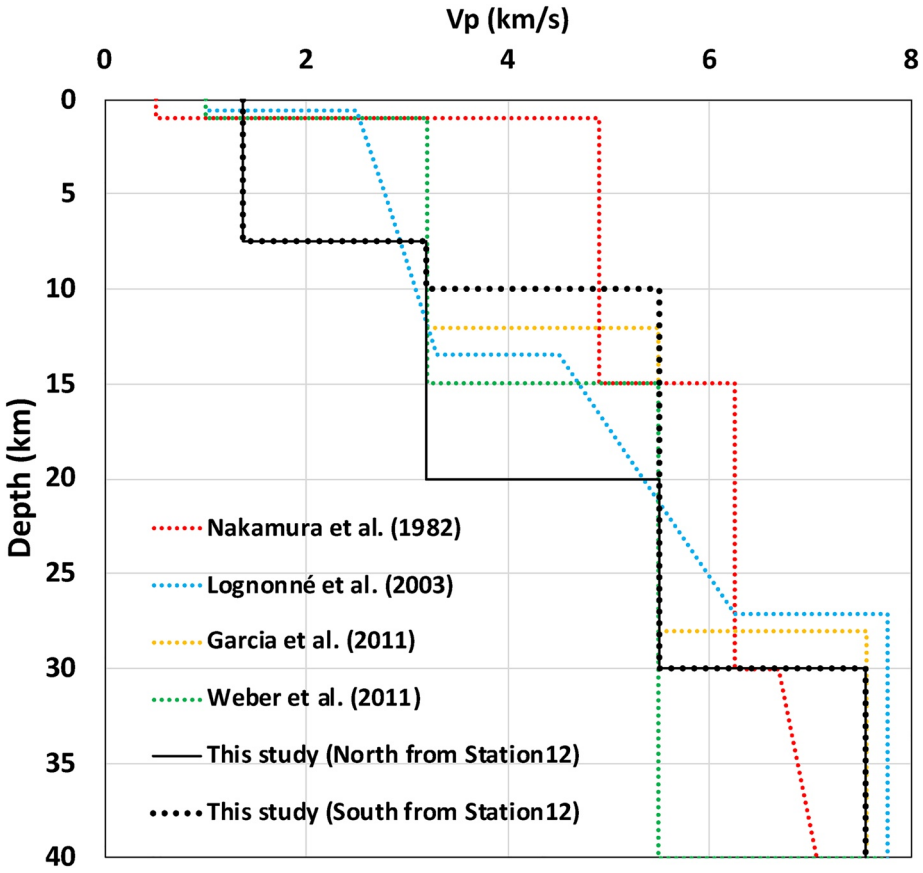

Figure 9. Comparison of crustal velocity structure. The horizontal axis shows P-wave velocity and the vertical axis shows depth from the surface. Note that each P-wave velocity is the averaged or median value. The black lines represent our models (solid: northern path, dotted: southern path), and the colored lines correspond to previously proposed models.

velocity structure in a different way. In other words, our numerical approach gives us an opportunity to interpret the lunar seismic data from the different point of view, helping us improve our knowledge on the seismic wave propagation within the Moon and the internal structure.

5. Conclusions

To constrain the subsurface scattering structure near Apollo 12 landing site, this study conducted two-dimensional simulations of seismic wave propagation under the lunar-like environment. From the parameter studies about the V_p/V_s ratio and the thickness of scattering layers, it turned out that our simulation successfully reproduced the seismic signals induced by the Apollo artificial impacts, thereby resulting in the constraint on scattering properties of the northern and southern region from Apollo 12 landing site. In these areas, it is considered that the scattering structure consists of two different scale heterogeneities. The first layer has 200 m scale scatterers and extends down to 7.5 km at both areas, and the second layer with 600 m scale heterogeneity underlies up to 20 km depth for the northern path and 10 km depth for the southern path, respectively. Combined with the geological viewpoints, it is estimated that the first layer reflects the scattering properties of basalt and ejecta blanket from Mare Imbrium, while the second layer corresponds to the heterogeneity within the underlying anorthosite crust.

As for velocity structure, our model requires the lower velocity for the first several km compared with those proposed before. However, while the previously proposed model covers wider ranges of regions, our structure shows the representative structure around Apollo 12 landing site. Thus, further numerical studies

enable us to discuss the general characteristics of lunar scattering layers as well as to investigate the lateral variation of heterogeneity within the lunar crust.

Concerning the elastic velocity ratio, it turned out that the smaller value (1.25 and 1.39 for the first and second layers, respectively) is necessary compared to those conventionally used (>1.73). Considering that the dry and porous samples show smaller velocity ratios, our result seems reasonable and consistent with the general picture of the lunar environment.

As this study conducted two-dimensional simulations, we solely focused on rise-coda part due to some constraints, such as geometrical attenuation. However, our future work will perform full three-dimensional simulations, hence allowing us to compare the simulated waves and the data for a longer period, including both rise- and decay-coda, which helps us expand the strategy for a better understanding of the heterogeneities within the lunar crust. In addition, since our method is applicable to other planetary bodies (e.g., Mars [Onodera et al., 2020]), this kind of forward approach would be a strong tool to support our interpretations in the field of planetary seismology.

Data Availability Statement

The Apollo seismic data used in this study were collected from Data Archives and Transmission System (DARTS) by the Center for Science-satellite Operation and Data Archive (C-SODA) of the Institute of Space and Astronautical Science of the Japan Aerospace Exploration Agency (https://darts.isas.jaxa.jp/planet/seismology/apollo/index.html). The maps were made with Generic Mapping Tool (GMT; Wessel & Smith, 1991). The relevant data analyzed in this study are found in GitHub repository (Onodera, 2020).

Acknowledgments
The authors would like to show great appreciation to JAXA Lunar and Planetary Exploration Data Analysis Group (JLPEDA), Research of Interior Structure and Evolution of Solar System Bodies Project (RISE) of National Astronomical Observatory of Japan, and Japan Agency for Marine-Earth Science and Technology (JAMSTEC) for providing us calculation resources. The authors are grateful to the Editor Laurent Montesi, Kuangdai Leng, Anne Obermann, Angela G Marusiak and an anonymous reviewer for providing us of fruitful advice, resulting in refining our study. The authors would also like to thank Enago (www.enago.jp) for the English language review.

References

Beyreuther, M., Barsch, R., Krischer, L., Megies, T., Behr, T., & Wassermann, J. (2010). ObsPy: A Python toolbox for seismology. *Seismological Research Letters*, *81*(3), 530–533. https://doi.org/10.1785/gssrl.81.3.530

Blanchette-Guertin, J. F., Johnson, C. L., & Lawrence, J. F. (2012). Investigation of scattering in lunar seismic coda. *Journal of Geophysical Research*, *117*. https://doi.org/10.1029/2011JE004042

Blanchette-Guertin, J. F., Johnson, C. L., & Lawrence, J. F. (2015). Modeling seismic energy propagation in highly scattering environments. *Journal of Geophysical Research: Planets*, *120*, 515–537. https://doi.org/10.1002/2014JE004654

Cooper, M. R., Kovach, R. L., & Watkins, J. S. (1974). Lunar near-surface structure. *Reviews of Geophysics and Space Physics*, *12*(3), 291–308. https://doi.org/10.1029/RG012i003p00291

Dainty, A. M., Toksöz, M. N., Anderson, K. R., Pines, P. J., Nakamura, Y., & Latham, G. (1974). Seismic scattering and shallow structure of the Moon in Oceanus Procellarum. *The Moon*, *9*(1–2), 11–29. https://doi.org/10.1007/BF00565388

Daubar, I. J., Lognonné, P., Teanby, N. A., Collins, G. S., Clinton, J., Stähler S., et al. (2020). A new crater near InSight: Implication for seismic impact detectability on Mars. *Journal of Geophysical Research: Planets*, *125*, ee2020JE006382. https://doi.org/10.1029/2020JE006382

Daubar, I., Lognonné, P., Teanby, N. A., Miljković, K., Stevanović, J., Vaubaillon, J., et al. (2018). Impact-seismic investigations of the InSight mission. *Space Science Reviews*, *214*, 132. https://doi.org/10.1007/s11214-018-0562-x

Gagnepain-Beyneix, J., Lognonné, P., Chenet, H., Lombardi, D., & Spohn, T. (2006). A seismic model of the lunar mantle and constraints on temperature and mineralogy. *Physics of the Earth and Planetary Interiors*, *159*(3–4), 140–166. https://doi.org/10.1016/j.pepi.2006.05.009

Garcia, R. F., Gagnepain-Beyneix, J., Chevrot, S., & Lognonné, P. (2011). Very preliminary reference Moon model. *Physics of the Earth and Planetary Interiors*, *188*(1–2), 96–113. https://doi.org/10.1016/j.pepi.2011.06.015

Gillet, K., Margerin, L., Calvet, M., & Monnereau, M. (2017). Scattering attenuation profile of the Moon: Implications for shallow moonquakes and the structure of the megaregolith. *Physics of the Earth and Planetary Interiors*, *262*, 28–40. https://doi.org/10.1016/j.pepi.2016.11.001

Gong, S., Wieczorek, M. A., Nimmo, F., Kiefer, W. S., Head, J. W., Huang C., et al. (2016). Thickness of mare basalts on the Moon from gravity and topography, *Journal of Geophysical Research: Planets*, *121*, 854–870. https://doi.org/10.1002/2016JE005008

Gudkova, T. V., Lognonné, P., & Gagnepain-Beyneix, J. (2011). Large impacts detected by the Apollo seismometers: Impactor mass and source cutoff frequency estimations. *Icarus*, *211*(2), 1049–1065. https://doi.org/10.1016/j.icarus.2010.10.028

Gudkova, T. V., Lognonné, P., Miljković, K., & Gagnepain-Beyneix, J. (2015). Impact cutoff frequency – Momentum scaling law inverted from Apollo seismic data. *Earth and Planetary Science Letters*, *427*, 57–65. https://doi.org/10.1016/j.epsl.2015.06.037

Han, S. C., Schmerr, N., Neumann, G., & Holmes, S. (2014). Global characteristics of porosity and density stratification within the lunar crust from GRAIL gravity and Lunar Orbiter Laser Altimeter topography data. *Geophysical Research Letters*, *41*, 1882–1889. https://doi.org/10.1002/2014GL059378

Hartmann, W. K. (1973). Ancient lunar mega-regolith and subsurface structure. *Icarus*, *18*(4), 634–636. https://doi.org/10.1016/0019-1035(73)90066-3

Hasse, I., Gläser, P., Knapmeyer, M., Oberst, J., & Robinson, M. S. (2013). Improved coordinates of the Apollo 17 lunar seismic profiling experiment (LPSE) components. In W. V., Boynton & T. J., Ahrens (Eds.), *Proceedings of the Lunar and Planetary Science Conference 44th* (pp. 1966).

Heffels, A., Knapmeyer, M., Oberst, J., & Haase, I. (2017). Re-evaluation of Apollo 17 lunar seismic profiling experiment data. *Planetary and Space Science*, *135*, 43–54. https://doi.org/10.1016/j.pss.2016.11.007

Heiken, G., Vaniman, D., & French, B. M. (1991). *Lunar sourcebook: A user's guide to the Moon*. Cambridge, England; New York, NY: Cambridge University Press.

Horvath, P. (1979). *Analysis of lunar seismic signals: Determination of instrumental parameters and seismic velocity distribution*. Doctoral Thesis of the University of Texas at Dallas.

Jaumann, R., Hiesinger, H., Anand, M., Crawford, I. A., Wagner, R., Sohl, F., et al. (2012). Geology, geochemistry, and geophysics of the Moon: Status of current understanding. *Planetary and Space Science*, *74*(1), 15–41. https://doi.org/10.1016/j.pss.2012.08.019

Kanamori, H., Mizutani, H., & Hamano, Y. (1971). Elastic wave velocities of Apollo 12 rocks at high pressure. In A. A. Levinson (Ed.), *Proceedings of the 2nd Lunar Science Conference* (Vol. *3*, pp. 2323–2326).

Kanamori, H., Nur, A., Chung, D., Wones, D., & Simmons, G. (1970). Elastic wave velocities of lunar samples at high pressures and their geophysical implications. *Science*, *167*(3918), 726–728. https://doi.org/10.1126/science.167.3918.726

Kawase, K. (2011). A general formula for calculating meridian arc length and its application to coordinate conversion in the Gauss-Krüger projection, *Geological Society of India Bulletin*, *59*, 1–13.

Khan, A., Mosegaard, K., & Rasmussen, K. L. (2000). A new seismic velocity model for the Moon from a Monte Carlo inversion of the Apollo lunar seismic data. *Geophysical Research Letters*, *27*(11), 1591–1594. https://doi.org/10.1029/1999GL008452

Kumagai, H., Saito, T., O'Brien, G., & Yamashina, T. (2011). Characterization of scattered seismic wavefields simulated in heterogeneous media with topography. *Journal of Geophysical Research*, *116*, B03308. https://doi.org/10.1029/2010JB007718

Latham, G., Ewing, M., Dorman, J., Press, F., Toksöz, N., Sutton, G., et al. (1970). Seismic data from man-made impacts on the Moon. *Science*, *170*(3958), 620–626. https://doi.org/10.1126/science.170.3958.620

Latham, G., Ewing, M., Press, F., Sutton, G., Dorman, J., Nakamura, Y., et al. (1971). Passive seismic experiment. In *Apollo 14 Preliminary Science Report* (pp. 133–160). NASA SP paper SP-272.

Lee, M. W. (2003). *Velocity ratio and its application to predicting velocities* (pp. 2197). US Geological Survey Bulletin.

Lognonné, P., Gagnepain-Beyneix, J., & Chenet, H. (2003). A new seismic model of the Moon: Implications for structure, thermal evolution and formation of the Moon. *Earth and Planetary Science Letters*, *211*(1–2), 27–44. https://doi.org/10.1016/S0012-821X(03)00172-9

Maeda, T., Takemura, S., & Furumura, T. (2017). OpenSWPC: An open-source integrated parallel simulation code for modeling seismic wave propagation in 3D heterogeneous viscoelastic media. *Earth Planets and Space*, *69*(1), 102. https://doi.org/10.1186/s40623-017-0687-2

McGetchin, T. R., Settle, M., & Head, J. W. (1973). Radial thickness variation in impact crater ejecta: Implications for lunar basin deposits. *Earth and Planetary Science Letters*, *20*(2), 226–236. https://doi.org/10.1016/0012-821X(73)90162-3

Melosh, H. J. (1989). Impact cratering – A geological process. In *11 of Oxford monographs on geology and geophysics*. Oxford: Oxford University Press.

Nakamura, Y., & Koyama, J. (1982). Seismic Q of the lunar upper mantle. *Journal of Geophysical Research: Solid Earth*, *87*(B6), 4855–4861. https://doi.org/10.1029/JB087iB06p04855

Nakamura, Y., Latham, G. V., & Dorman, H. J. (1983). Apollo Lunar seismic experiment – Final summary. *Journal of Geophysical Research*, *87*(S01). https://doi.org/10.1029/JB087iS01p0A117

Onodera, K. (2020). *Onodera0726/Onodera_JGR2020-ver1.2*, GitHub Data Repository. https://doi.org/10.5281/zenodo.4286059

Onodera, K., Kawamura, T., Ishihara, Y., Maeda, T., & Tanaka, S. (2018). Evaluation of the effect of surface and Moho topographies on lunar seismic wave propagation. In *Proceedings of the Lunar and Planetary Science Conference* (Vol. *49*, pp. 1692).

Onodera, K., Kawamura, T., Lucas, A., Perrin, C., Rodriguez, S., Drilleau, M., et al. (2020). Seismic wave modeling of a Martian dust devil constrained by multi-observation data. In *Proceedings of the Lunar and Planetary Science Conference* (Vol. *51*, pp. 1279).

Sato, H., Fehler, M., & Maeda, T. (2012). *Seismic wave propagation and scattering in the heterogeneous earth structure* (2nd ed.). Springer-Verlag.

Swann, G., Bailey, N., Batson, R., Eggleton, R., Hait, M., Holt, H., et al. (1971). Preliminary geologic investigations of the Apollo 14 landing site, In *Apollo 14 Preliminary Science Report* (pp. 39–85). NASA SP paper SP-272.

Takemura, S., Furumura, T., & Maeda, T. (2015). Scattering of high-frequency seismic waves caused by irregular surface topography and small-scale velocity inhomogeneity. *Geophysical Journal International*, *201*(1), 459–474. https://doi.org/10.1093/gji/ggv038

Teanby, N. A., & Wookey, J. (2011). Seismic detection of meteorite impacts on Mars. *Physics of the Earth and Planetary Interiors*, *186*(1–2), 70–80. https://doi.org/10.1016/j.pepi.2011.03.004

Toksöz, N., Dainty, A. M., Solomon, S. C., & Anderson, K. R. (1974). Structure of the Moon. *Reviews of Geophysics and Space Physics*, *12*(4), 539–567. https://doi.org/10.1029/RG012i004p00539

Wagner, R. V., Nelson, D. M., Plescia, J. B., Robinson, M. S., Speyerer, E. J., Mazarico, E. (2017). Coordinates of anthropogenic features on the Moon. *Icarus*, *283*, 92–103. https://doi.org/10.1016/j.icarus.2016.05.011

Weber, R. C., Knapmeyer, M., Panning, M., & Schmerr, N. (2015). Chapter 10. Modeling approaches in planetary seismology. In *Extraterrestrial seismology* (pp. 140–155). Cambridge: Cambridge University Press.

Weber, R. C., Lin, P. Y., Garnero, E. J., Williams, Q., & Lognonné, P. (2011). Seismic detection of the lunar core. *Science*, *331*(6015), 309–312. https://doi.org/10.1126/science.1199375

Wessel, P., & Smith, W. H. F. (1991). Free software helps map and display data. *Eos, Transactions American Geophysical Union*, *72*(41), 441–448. https://doi.org/10.1029/90EO00319

Wieczorek, M. A., Neumann, G. A., Nimmo, F., Kiefer, W. S., Taylor, G. J., Melosh, H. J., et al. (2013). The crust of the Moon as seen by GRAIL. *Science*, *339*(6120), 671–675. https://doi.org/10.1126/science.1231530

Yamamoto, Y., Yamada, R., Ishihara, Y., Nakamura, Y., & Ishikawa, H. (2019). Apollo seismic data analysis in Python: ObsPy module and response function. In *Proceedings of the Lunar and Planetary Science Conference* (Vol. *50*, pp. 2492).

References From the Supporting Information

Takenaka, H., Komatsu, M., Toyokuni, G., Nakamura, T., & Okamoto, T. (2017). Quasi-Cartesian finite-difference computation of seismic wave propagation for a three-dimensional sub-global model. *Earth Planets and Space*, *69*(1), 67. https://doi.org/10.1186/s40623-017-0651-1

Nakamura, Y. (2011). Timing problem with the Lunar Module impact data as recorded by the LSPE and corrected near-surface structure at the Apollo 17 landing site. *Journal of Geophysical Research*, *116*(E12), E12005. https://doi.org/10.1029/2011JE003972